Journal of Electroanalytical Chemistry 999 (2025) 119559

Contents lists available at ScienceDirect

Journal of Electroanalytical Chemistry

journal homepage: www.elsevier.com/locate/jelechem

Ternary WO_3–MnO_2@SiNWs hybrid electrodes for high-performance Micro-supercapacitors with enhanced energy density and stability

Khadidja Boukhouidem [a,b,c,*], Amel Slimani [a,c,d], Khaled Derkaoui [e,*], Theodore Azemtsop Manfo [f,*], Toufik Hadjersi [b], Amar Manseri [b], Noureddine Selmi [g], Seddik Elhak Abaidia [a]

[a] Environmental,Materials,and Revetment Laboratory (EM-RL),M'Hamed Bougara University,Boumerdes 35000,Algeria
[b] Research Center on Semiconductors Technology for Energetic,CRTSE, Bd.Dr.Frantz Fanon, Box 140,7 Merveilles, Algiers 16038, Algeria
[c] M'Hamed Bougara University,Department of Physics,Boumerdes 35000, Algeria
[d] Research Unit Materials Processes and Environment,University of Boumerdes,Boumerdes, Algeria
[e] Centre de Développement des Technologies Avancées,Alger, Baba Hassen,Algeria
[f] Department of Electrical Engineering and Energy Technology,School of Technology and Innovation,University of Vaasa,Wolffintie 32, 65200 Vaasa,Finland
[g] Nuclear Research Centre of Birine (CRNB),Ain Oussera,Djelfa,Algeria

ARTICLE INFO

Keywords:
Silicon nanowires
Tungsten trioxide
Manganese dioxide
Composites
Electrode
Micro-supercapacitors

ABSTRACT

Advanced energy storage technologies, such as rechargeable Batteries and Micro-supercapacitors (μSCs) play a pivotal role in addressing the growing global energy demand. Improving their energy and power densities requires the development of electrode materials with well-engineered, hierarchical porous architectures. In this work, we report a facile hydrothermal synthesis of WO_3-MnO_2 composite nanostructures directly integrated onto silicon nanowires (SiNWs), which serve as a highly conductive and high-surface-area scaffold. The influence of annealing temperature on the structural, morphological, and electrochemical properties of the WO_3-MnO_2@-SiNWs composite was systematically investigated. Structural characterization through X-ray diffraction (XRD) and surface analysis via X-ray photoelectron spectroscopy (XPS) confirmed the successful formation of the hybrid oxide network. Furthermore, scanning electron microscopy (SEM) revealed a homogeneous distribution of the nanostructured composite coating over the vertically aligned SiNWs, forming a porous, interconnected network favorable for ion diffusion. Energy-dispersive X-ray spectroscopy (EDX) mapping confirmed the uniform presence of W, Mn, O, and Si elements throughout the electrode, indicating successful and consistent deposition of the WO_3-MnO_2 layers. The optimized electrode exhibited excellent capacitive performance, delivering a specific capacitance (Csp) of 16.56 $mF{\cdot}cm^{-2}$, an energy density (Ed) of 0.0001 $Wh{\cdot}cm^{-2}$, and a power density (Pd) of 0.024 $W{\cdot}cm^{-2}$, along with long-term cycling stability retaining 84 % of its initial capacitance over 4000 charge–discharge cycles. Additionally, electrochemical impedance spectroscopy revealed a consistent Csp of 14.23 $mF{\cdot}cm^{-2}$ over a wide frequency range (0.01 Hz–1 MHz), indicating efficient charge transfer and low internal resistance. A solid-state symmetric μSC device constructed using WO_3-MnO_2@SiNWs electrodes further demonstrated impressive performance, achieving a maximum specific capacitance of 96 $mF{\cdot}cm^{-2}$ at a scan rate of 2 $mV{\cdot}s^{-1}$, with 85 % capacitance retention over 2300 cycles and an energy density of 0.0028 $Wh{\cdot}cm^{-2}$ at a power density of 0.4 $W{\cdot}cm^{-2}$. These remarkable electrochemical properties are attributed to the synergistic effects of multivalent WO_3 and MnO_2 species combined with the high conductivity and mechanical stability of the SiNWs framework, highlighting the potential of this composite architecture for next-generation on-chip energy storage devices.

1. Introduction

Energy supply is necessary for modern society to function [1–4]. The global transition toward renewable energy sources, including solar and wind, has heightened the demand for efficient and scalable energy storage technologies to address their inherent intermittency [5,6].

* Corresponding authors.
E-mail addresses: k.boukhouidem@univ-boumerdes.dz (K. Boukhouidem), kderkaoui@cdta.dz (K. Derkaoui), theodore.azemtsop.manfo@uwasa.fi (T.A. Manfo).

https://doi.org/10.1016/j.jelechem.2025.119559
Received 23 July 2025; Received in revised form 13 October 2025; Accepted 15 October 2025
Available online 18 October 2025

Energy storage encompasses a variety of energy technologies, sizes, and applications. There are various ways of electrical energy storage (EES), such as chemical, thermal, mechanical, electrical, and electrochemical systems [7,8]. Over the past decade, portable electronic systems have advanced dramatically with new sensors and flexible electronics [9,10]. Portable energy storage solutions, such as batteries, fuel cells, and supercapacitors (SCs), are becoming more significant [11]. SCs have attracted research interest as power sources because of their high specific power and long cycle life when compared to rechargeable batteries [12]. Among the emerging candidates, micro-supercapacitors (μSCs) have drawn increasing attention due to their high-power density, rapid charge–discharge rates, long cycle life, and potential for integration into compact electronic systems [13–15]. However, balancing high energy density with long-term cycling stability remains a key challenge in the development of next-generation μSCs.

Transition metal oxides (TMOs) are widely explored as electrode materials owing to their multivalent redox behavior and high theoretical capacitance [16,17]. Tungsten trioxide (WO_3) offers excellent chemical stability and corrosion resistance along with pseudocapacitive characteristics [18–20] [8–10]. Despite these merits, its relatively low intrinsic electrical conductivity and moderate rate performance necessitate compositional or structural modification [21,22].

In this context, manganese dioxide (MnO_2) represents an attractive complement. Known for its environmental benignity, low cost, and high pseudocapacitance, MnO_2 exhibits fast surface-controlled redox activity that can effectively enhance the charge storage characteristics of hybrid systems [23–25]. When coupled with WO_3, the resulting heterostructure can leverage the synergistic advantages of both oxides—combining the stable redox chemistry of WO_3 with the rapid kinetics of MnO_2 to improve capacitance, rate performance, and structural durability [26–28].

Silicon nanowires (SiNWs) are widely recognized as an ideal scaffold for advanced electrode architectures due to their high surface-to-volume ratio, excellent electrical conductivity, and mechanical robustness, which collectively provide abundant active sites and efficient charge transport pathways [29,30]. Their vertical alignment ensures intimate contact with deposited oxides, facilitating rapid ion diffusion and electron transfer, while their inherent compatibility with CMOS technology makes them particularly attractive for on-chip micro-supercapacitor applications [31,32]. In addition, the binder-free integration of transition metal oxides onto SiNWs reduces interfacial resistance and enhances structural stability. In recent years, silicon nanowires (SiNWs) have emerged as a versatile platform for supercapacitor electrodes thanks to their large surface area, conductivity, and compatibility with Si-based microelectronics. Significant progress has been made by combining SiNWs with transition-metal compounds and conductive polymers to overcome their intrinsic limitations. For instance, MnO_2/PEDOT–rGO–Ag hybrids on SiNWs exhibited enhanced capacitance and cycling stability [33], while hierarchical SiNW/PEDOT@Pt/MnOx structures achieved a record areal capacitance of 352.08 $mF{\cdot}cm^{-2}$ [34]. More recently, polypyrrole/Ni–Co sulfide co-deposited on Ni-passivated SiNWs delivered a remarkable 1602 $F{\cdot}g^{-1}$ with excellent long-term retention [1]. These studies clearly highlight the pivotal role of SiNWs as scaffolds that, when combined with functional nanomaterials, enable the design of high-performance and durable supercapacitor electrodes.

Recent studies have reported hybrid structures based on either WO_3 or MnO_2 combined with SiNWs, yet most of these approaches still rely on conductive additives or involve complex fabrication steps [34–36]. In contrast, our work proposes a simple, low-cost route for fabricating a ternary WO_3–MnO_2 nanocomposite directly on SiNWs grown via electroless metal-assisted chemical etching. This binder-free architecture ensures intimate contact between the nanostructured oxides and the conductive silicon backbone, promoting efficient charge transport and mechanical integrity.

Furthermore, the influence of post-deposition thermal annealing on the structural and electrochemical properties of such hybrid systems remains underexplored. Annealing can significantly affect crystallinity, interface quality, and electrochemical activity by tuning the phase composition and surface structure of the composite [37–39]. SiNWs cause solvent exclusion from pores and prevent the pore surface from becoming an active capacitive site [40]. In this study, we demonstrate that optimized thermal treatment at 573 K enhances the crystallinity of the oxides and passivates the SiNW surface, thereby improving cycling stability and performance in aqueous Na_2SO_4 electrolyte.

We report here the synthesis and characterization of a novel WO_3–MnO_2@SiNWs hybrid electrode fabricated via hydrothermal deposition followed by thermal annealing. The resulting architecture offers enhanced areal capacitance, energy density, and long-term stability without the use of conductive carbon materials. The electrochemical properties were systematically assessed using cyclic voltammetry (CV), galvanostatic charge–discharge (GCD), and electrochemical impedance spectroscopy (EIS), revealing the strong potential of this system for integrated micro-supercapacitor applications.

2. Materials and methods

2.1. Materials

Silicon wafers with (100) orientation were obtained from Sil'tronix. All reagents employed were of analytical grade and used without further purification. Sigma-Aldrich supplied the following chemicals: hydrogen peroxide (H_2O_2, 30 %), hydrofluoric acid (HF, 40 %), nitric acid (HNO_3, 65 %), silver nitrate ($AgNO_3$, extra pure), potassium permanganate ($KMnO_4$), sodium tungstate dihydrate ($Na_2WO_4{\cdot}2H_2O$), sodium sulfate (Na_2SO_4), hydrochloric acid (HCl, 37 %), and sulfuric acid (H_2SO_4). The resistivity of the deionized water (DIW) used in this study was 18 MΩ·cm.

2.2. Sample preparation

2.2.1. Preparation of silicon nanowire arrays

Highly conductive silicon nanowires (SiNWs) were fabricated from p-type silicon wafers exhibiting very low resistivity (0.015–0.024 Ω·cm). A single-step silver-assisted chemical etching method was employed to achieve well-structured and porous SiNWs [30]. Initially, square substrates (1 cm × 1 cm) were subjected to degreasing in acetone and ethanol, followed by thorough rinsing in deionized water. Organic residues were removed by immersing the substrates in a freshly prepared piranha solution (H_2SO_4:H_2O_2 = 3:1) for 15 min. Afterward, the samples were rinsed again with deionized water and dried under a nitrogen flow. To eliminate the native oxide layer, the cleaned wafers were dipped in a 10 % hydrofluoric acid (HF) solution, rinsed, and nitrogen-dried. Etching was then performed in an aqueous solution containing 5 M HF and 0.5 M $AgNO_3$ at 60 °C for 60 min to produce vertically aligned SiNWs. Post-etching, the samples were immersed in concentrated nitric acid (HNO_3) for 5 min to dissolve residual silver particles, followed by a final rinse with deionized water and drying under nitrogen gas. The optimized metal-assisted chemical etching time for SiNW fabrication was fixed at 1 h, which yields nanowires with an average length of about 32 μm. As shown in our earlier study (Derkaoui et al. [31]), extending the etching beyond 1 h leads to tip degradation and nanowire agglomeration caused by Coulombic interactions, thereby decreasing the effective surface area, while shorter etching times result in significantly reduced nanowire length and limited active surface. These optimized conditions were adopted in the present work to ensure high structural integrity and surface availability for subsequent oxide deposition.

2.2.2. Hydrothermal deposition of the WO3-MnO2 composites on silicon nanowires

As depicted in Fig. S1, the hydrothermal technique proves to be an effective approach for synthesizing composite materials. In this work, WO_3–MnO_2 composite films were directly grown on silicon nanowire

(SiNW) substrates via a controlled hydrothermal process. To begin, 0.1 M sodium tungstate dihydrate ($Na_2WO_4 \cdot 2H_2O$) was dissolved in 12.5 mL of deionized water (DIW) and subjected to ultrasonication for approximately 10 min to ensure complete dissolution. A separate solution of 0.1 M potassium permanganate ($KMnO_4$, 12.5 mL) was then added slowly, dropwise, under continuous magnetic stirring at ambient temperature. The pH of the resulting mixture was carefully adjusted to approximately 2.0 by gradually introducing a 3 M hydrochloric acid (HCl) solution, forming a stable suspension.

The prepared mixture was transferred into a 50 mL Teflon-lined stainless-steel autoclave containing a pre-cleaned SiNW substrate (1 × 1 cm^2). The sealed autoclave was then placed in an oven and maintained at 453 K for 2 h. Upon completion, the system was allowed to cool naturally to room temperature. The resulting WO_3–MnO_2-coated SiNWs were retrieved, thoroughly rinsed with DIW to eliminate unbound particles, and dried in an oven at 353 K for 1 h. Composite films with varying structural properties were obtained by annealing at different temperatures—namely, unannealed, 473 K, 573 K, and 673 K—while keeping all other synthesis parameters constant. These samples were designated as A, B, C, and D, respectively.

The hydrothermal reaction can be summarized by the following chemical equation:

$$Na2WO4,2H2O + 2\,KMnO4 + 2\,HCl\ WO3{-}2MnO2\ (composite) + 2\,NaCl + 2KCl + 3H2O + 2O2\uparrow \quad (1)$$

The areal mass loading of the deposited WO_3–MnO_2 active layer on the SiNWs was determined by measuring the weight difference of the substrate before and after deposition using a high-precision microbalance. The resulting loading was approximately 30 $\mu g \cdot cm^{-2}$, which ensures an optimal balance between sufficient active material for high electrochemical performance and efficient ion accessibility without inducing diffusion limitations.

2.3. Characterization techniques

The WO_3–MnO_2/SiNWs composite thin films were thoroughly characterized using a combination of physicochemical techniques to investigate their structural, morphological, and compositional properties. The surface topography and elemental distribution were examined using field emission scanning electron microscopy (FE-SEM, JEOL JSM-6360) equipped with energy-dispersive X-ray spectroscopy (EDX). Crystallographic analysis was carried out by X-ray diffraction (XRD) using a PANalytical X'Pert Pro diffractometer with Cu Kα radiation ($\lambda = 1.5418$ Å), covering a 2θ range from 10° to 90°. Additionally, surface chemical composition and oxidation states of the constituent elements were assessed via X-ray photoelectron spectroscopy (XPS), using an ESCALAB 250Xi instrument. This technique operates by irradiating the sample with X-rays and analyzing the kinetic energy of emitted photoelectrons to determine surface elemental composition and chemical bonding environments.

2.4. Electrochemical measurements

All electrochemical measurements were performed using a Metrohm-Autolab PGSTAT 128 N workstation in 1 M Na_2SO_4 aqueous electrolyte at room temperature. A three-electrode configuration was used for electrode-level analysis, where the WO_3–MnO_2@SiNWs sample served as the working electrode, platinum foil as the counter electrode, and a saturated Ag/AgCl as the reference electrode. A two-electrode configuration was employed for symmetric device evaluation. The active electrode surface in contact with the electrolyte was approximately 0.49 cm^2, and silver paste ensured good electrical contact with the current collector.

Cyclic voltammetry (CV), galvanostatic charge–discharge (GCD), and electrochemical impedance spectroscopy (EIS) were employed to evaluate electrochemical behavior. EIS measurements were conducted in the frequency range of 0.01 Hz to 1 MHz.

The areal-specific capacitance (Csp, in $mF \cdot cm^{-2}$) from CV data was calculated using Eq. (2) [41]:

$$C_{sp} = \frac{\int_{Ua}^{Ub} I\,dv}{2 \times v \times S \times (Ub - Ua)} \quad (2)$$

Where IdV is the integrated area of one CV cycle, v is the potential sweep rate, S is the surface area, and Ua and Ub are the lowest and highest potential, respectively.

From GCD curves, C_{sp} was obtained using Eq. (3) [41]:

$$C_{sp} = I\Delta td/S \times \Delta U \quad (3)$$

Where I (mA) is the discharge current, Δtd (s) is the discharge time, and ΔU (V) is the potential window.

The energy density E ($Wh \cdot cm^{-2}$) and power density P ($W \cdot cm^{-2}$) were estimated using Eqs. (4) and (5), respectively [31]:

$$E = 1/2 \times (C_{sp} \times \Delta U^2) \quad (4)$$

$$P = E/\Delta td \quad (5)$$

Capacitance at low frequency was also estimated from EIS using the following relation [41]:

$$Csp = -1/2\pi f\, Z'' S \quad (6)$$

Where f is the frequency and Z″ is the low-frequency imaginary part of Z.

3. Results and discussion

X-ray diffraction (XRD) was employed to investigate the crystallographic structure and phase composition of the WO_3–MnO_2 composite thin films, as shown in Fig. 1. The samples labeled A, B, C, and D exhibited well-defined diffraction peaks corresponding to characteristic reflections of WO_3 and α-MnO_2, confirming the successful formation of the composite. Specifically, peaks attributed to WO_3 were indexed to the (100), (001), (110), (101), (201), (202), (400), and (401) planes in agreement with the JCPDS card No. 75–2187, while α-MnO_2 reflections were assigned to the (110) and (5 1–1) planes based on JCPDS card No. 24–0735. These results indicate the coexistence of hexagonal WO_3 and tetragonal MnO_2 phases in the films. The XRD analysis of sample A, which did not undergo thermal treatment, reveals predominantly weak and broad diffraction peaks, indicative of a poorly crystalline structure. Annealing at 473 K and 573 K leads to a pronounced increase in the intensity of the diffraction peaks corresponding to WO_3 and MnO_2, indicating a significant improvement in the crystallinity of the composite structure. However, when the annealing temperature is raised to 673 K, a decline in peak intensity occurs, likely resulting from structural degradation or partial collapse of the nanowire matrix due to thermal stress, a hypothesis corroborated by morphological alterations observed via SEM. Furthermore, the detection of minor peaks attributed to hydrated tungsten oxide phases (such as β-$H_{3.32}O_{0.66}W_1$ and δ-$H_2O_{1.5}W_1$)

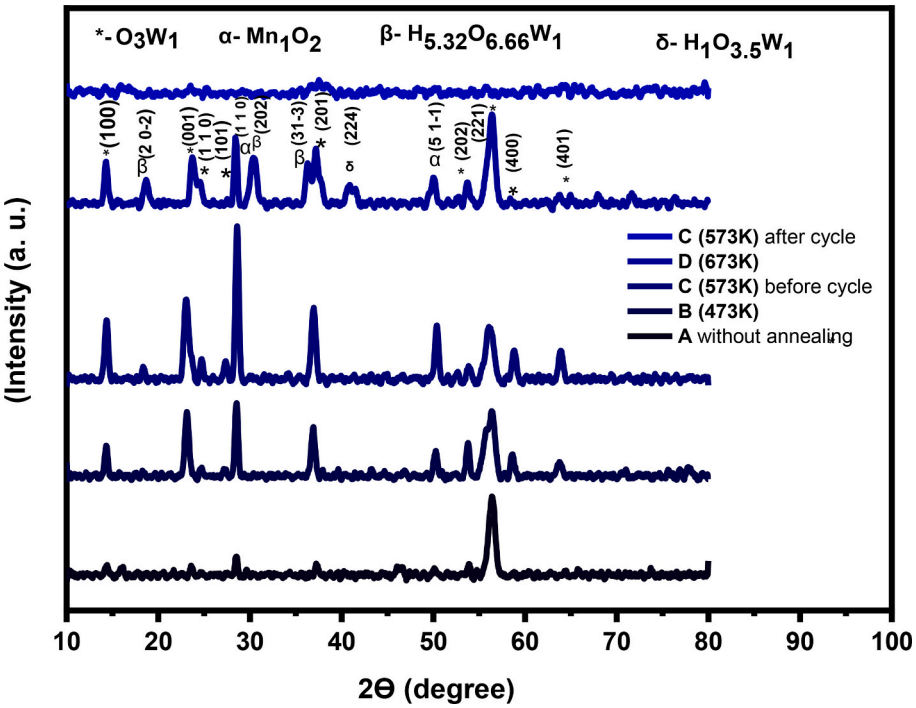

Fig. 1. XRD patterns of WO_3–MnO_2/SiNWs composite thin films: (A) as-prepared (unannealed), and annealed at (B) 473 K, (C) 573 K, and (D) 673 K. The pattern labeled (C) corresponds to the sample annealed at 573 K after electrochemical cycling.

suggests the formation of a structurally complex composite, which may facilitate synergistic electrochemical behavior and enhanced charge storage performance. XRD patterns of sample C, recorded before and after electrochemical cycling, exhibit a pronounced decrease in diffraction peak intensity, pointing to partial dissolution or structural breakdown of the SiNWs scaffold. This structural degradation is further evidenced by SEM imaging, which reveals substantial deterioration in nanowire morphology after extended cycling. To further quantify the structural changes, the average crystallite sizes of the WO_3 and MnO_2 phases were calculated from the main diffraction peaks using the Scherrer Eq. [31]. In addition, lattice parameters were estimated for the hexagonal WO_3 and tetragonal MnO_2 phases by applying the corresponding Bragg Eqs. [31]. The obtained values are summarized in **Table 1**. The data provide valuable insight into the structural evolution of the WO_3–MnO_2/SiNWs nanocomposites as a function of annealing temperature. For the unannealed sample (A), both WO_3 and MnO_2 phases exhibit small crystallite sizes (~14 and ~ 11 nm, respectively) and relatively broad diffraction peaks, which is consistent with poor crystallinity and structural disorder. Upon annealing at 473 K (sample B), the crystallite sizes increase markedly to ~21 nm for WO_3 and ~ 18 nm for MnO_2, reflecting the onset of grain growth and improved long-range ordering. The most significant enhancement is observed at 573 K (sample C), where WO_3 and MnO_2 reach average crystallite sizes of ~27 and ~ 23 nm, respectively. This optimum thermal treatment not only enhances crystallinity but also stabilizes the lattice parameters, suggesting improved structural coherence and reduced defect density. Such features are expected to facilitate faster electron transport and ion intercalation, thereby explaining the superior electrochemical performance observed for this sample. However, further increasing the annealing temperature to 673 K (sample D) leads to a reduction in crystallite size and slight lattice expansion ($a \approx 7.38$ Å, $c \approx 3.95$ Å for WO_3), which can be attributed to structural degradation, thermal stress, or partial collapse of the nanowire scaffold. These findings highlight a clear correlation between annealing temperature, crystallite size, and structural stability: moderate thermal treatment enhances crystallinity and electrochemical activity, while excessive heating induces structural deterioration that compromises performance. Overall, the observed crystalline features and the thermal stability of these hybrid nanostructures underscore their potential for application in robust, high-efficiency micro-supercapacitor electrodes.

Scanning Electron Microscopy (SEM) was employed to investigate the surface morphology and structural arrangement of the synthesized silicon nanowires (SiNWs) before the deposition of the WO_3–MnO_2 composite. As shown in Fig. 2, the top-view SEM images (Fig. 2a and b) reveal that the SiNWs form a densely packed and highly porous network. This pronounced porosity significantly increases the available surface area, which is advantageous for subsequent material coating and electrochemical performance. At higher magnification (Fig. 2b), the tips of the nanowires are observed to lean and interconnect, potentially improving both mechanical cohesion and electrical pathways within the

Table 1
Calculated lattice parameters and crystallite sizes of WO_3–MnO_2/SiNWs nanocomposites at different annealing temperatures.

Sample	Phase	Lattice parameters (Å)	Crystallite size (nm)	Remarks
A (Unannealed)	WO_3 (hexagonal)	$a \approx 7.34$, $c \approx 3.92$	~14	Poorly crystalline, broad peaks
	MnO_2 (tetragonal)	$a \approx 9.78$, $c \approx 2.86$	~11	Low crystallinity
B (473 K)	WO_3 (hexagonal)	$a \approx 7.35$, $c \approx 3.94$	~21	Enhanced crystallinity
	MnO_2 (tetragonal)	$a \approx 9.79$, $c \approx 2.87$	~18	Improved ordering
C (573 K)	WO_3 (hexagonal)	$a \approx 7.36$, $c \approx 3.94$	~27	Optimum crystallinity
	MnO_2 (tetragonal)	$a \approx 9.80$, $c \approx 2.88$	~23	Highest stability
D (673 K)	WO_3 (hexagonal)	$a \approx 7.38$, $c \approx 3.95$	~19	Slight coarsening, degradation
	MnO_2 (tetragonal)	$a \approx 9.82$, $c \approx 2.89$	~16	Structural deterioration

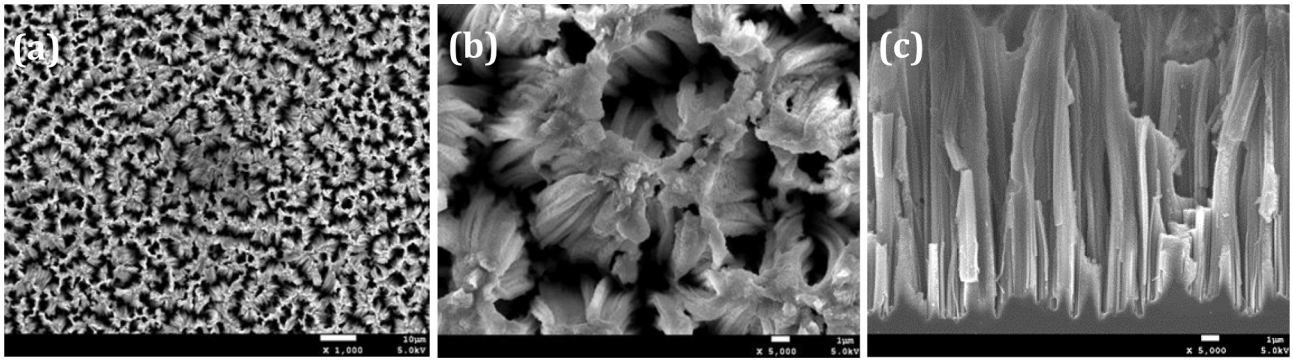

Fig. 2. SEM images of SiNWs on Si substrate: (a) and (b) top-view images showing dense nanowire morphology with porosity; (c) cross-sectional view highlighting the vertical alignment and uniform length of the nanowires.

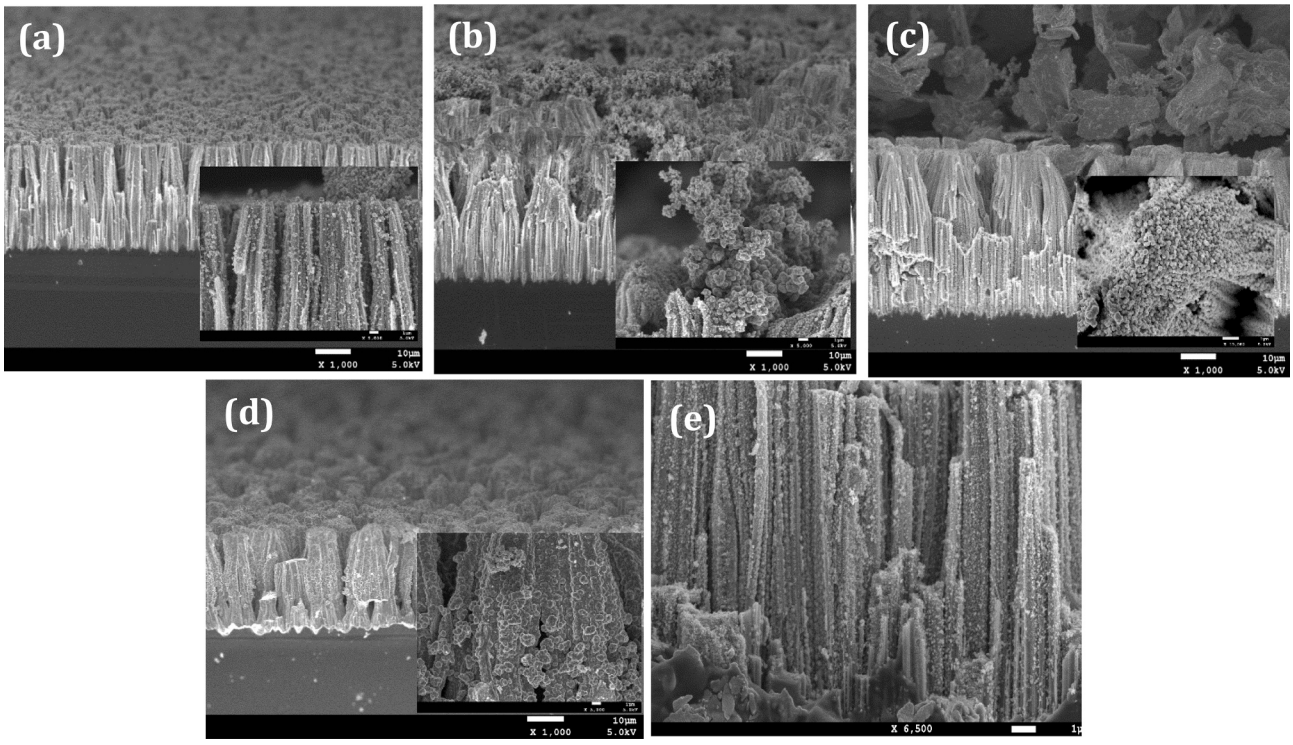

Fig. 3. SEM images of WO_3–MnO_2/SiNWs composite films: (a) sample A (unannealed), (b) sample B (annealed at 473 K), (c) sample C (annealed at 573 K), and (d) sample D (annealed at 673 K). Image (e) shows the morphology of sample C after electrochemical cycling.

composite. The cross-sectional image (Fig. 2c) confirms a vertically aligned nanowire array with consistent length and only minor variation in diameter. Such vertical orientation is essential for promoting efficient electron and ion transport, thereby enhancing the performance of the final μSCs device. Overall, the observed structural features highlight the suitability of SiNWs as a robust and high-surface-area scaffold for functional composite integration.

The SEM images in Fig. 3 highlight the morphological evolution of WO_3–MnO_2 composites deposited on silicon nanowires (SiNWs) and subjected to different annealing temperatures. In the unannealed sample (Fig. 3**a**); the SiNWs are uniformly coated with a continuous layer of coarse granular material, suggesting a dense and disordered film structure. As the annealing temperature increases from 473 K to 673 K (Figs. 3 **b–d)**, a noticeable reduction in nanowire density is observed. This phenomenon is likely due to thermal-induced stress generated during the crystallization of the WO_3–MnO_2 layer, which may cause partial breakage or collapse of the nanowires.

Additionally, excessive oxide deposition is evident in **Fig. 3b** and **c**, indicating a non-uniform growth that may lead to agglomeration and affect the film's porosity. After electrochemical cycling (Fig. 3**e**), a slight further decrease in nanowire density is detected, attributed to partial dissolution or structural degradation in the electrolyte environment. Despite these changes, the overall architecture remains intact, underscoring the mechanical resilience of the composite and its suitability for μSCs applications.

This hierarchical structure promotes efficient ion transport by minimizing diffusion paths and providing abundant electrochemically active sites, thereby enhancing redox kinetics. The annealing temperature plays a critical role in tuning the film's surface texture and structural coherence, which directly impacts its charge storage capacity and long-term performance in energy storage devices.

Energy-dispersive X-ray spectroscopy (EDX) was employed to analyze the elemental composition and spatial distribution within the WO_3–MnO_2/SiNWs composite annealed at 573 K. As shown in Fig. 4a, the EDX elemental mapping reveals a uniform and homogeneous distribution of oxygen (O), manganese (Mn), tungsten (W), and silicon (Si)

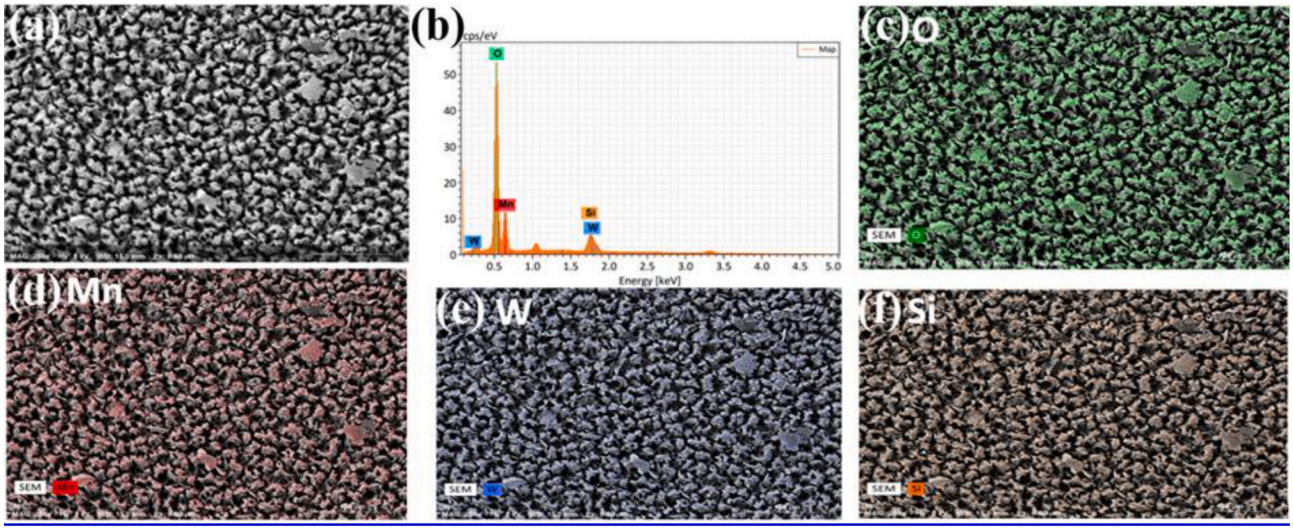

Fig. 4. (a) SEM image of sample B annealed at 473 K. (b) Corresponding energy-dispersive X-ray (EDX) spectrum confirming the elemental composition. (c–f) Elemental mapping showing the spatial distribution of (c) oxygen (green), (d) manganese (red), (e) tungsten (blue), and (f) silicon (orange), demonstrating uniform dispersion of WO_3–MnO_2 components on the SiNW substrate. (For interpretation of the references to colour in this figure legend, the reader is referred to the web version of this article.)

across the surface of the nanowires. This even dispersion suggests successful integration of WO_3 and MnO_2 components within the composite matrix. The corresponding EDX spectrum (Fig. 4b) exhibits characteristic peaks for O, Mn, W, and Si, confirming the presence of these elements in the sample. The individual elemental maps presented in Figs. 4c-f (O in green, Mn in red, W in blue, and Si in orange) further demonstrate the consistent distribution of each constituent throughout the composite. This uniformity is essential for ensuring efficient electron and ion transport during electrochemical operation, thereby contributing to improved performance and stability of the electrode in supercapacitor applications.

Quantitative EDX analysis was carried out to determine the elemental composition of the WO_3–MnO_2/SiNWs composite. The obtained atomic percentages are summarized in **Table 2**. The results indicate that manganese and tungsten are present in nearly equimolar proportions, with Mn and W atomic contents of 17.3 % and 16.4 %, respectively, corresponding to a Mn/W atomic ratio of approximately **1.05**. This ratio is in excellent agreement with the equimolar precursor ratio used during synthesis, confirming that both transition-metal oxides were successfully and homogeneously incorporated into the nanocomposite matrix. The balanced composition and uniform elemental distribution contribute to the synergistic redox behavior of the composite, facilitating efficient charge transfer and enhanced electrochemical performance.

X-ray photoelectron spectroscopy (XPS) was conducted on the optimized WO_3–MnO_2/SiNWs composite (annealed at 573 K) to investigate its surface composition and chemical states (Fig. 5). The survey spectrum (Fig. 5a) confirms the presence of Mn, W, and O, along with a minor signal from carbon, which is commonly associated with ambient contamination or adventitious carbon.

A notable feature in the XPS survey is the appearance of a distinct peak around 1000 eV, which corresponds to the W NOO Auger transition. This Auger signal, characteristic of tungsten compounds, complements the W 4f core-level peaks typically observed between 35 and 40 eV and provides further evidence for the presence of tungsten in an oxidized state [42]. Such high-binding-energy Auger peaks arise from multi-electron relaxation processes following photoionization and are frequently used to refine chemical state analysis in transition metal oxides. In particular, the W NOO Auger peak is sensitive to the oxidation state and local chemical environment of tungsten, making it a valuable indicator for the identification and confirmation of WO_3 within the hybrid material.

The high-resolution Mn 2p spectrum (Fig. 5b) displays two prominent peaks located at 642.6 eV and 654.0 eV, which correspond to Mn $2p_{3/2}$ and Mn $2p_{1/2}$, respectively—features characteristic of Mn^{4+} species in MnO_2. Additional satellite features at 645.3 eV and 656.5 eV indicate the presence of lower oxidation states such as Mn^{2+} or Mn^{3+}, suggesting a degree of redox heterogeneity and non-stoichiometry within the manganese oxide layer [43]. Such mixed valence states are often associated with enhanced pseudocapacitive behavior due to multiple accessible redox reactions.

In the W 4f region (Fig. 5c), the main doublet peaks at 35.2 eV and 37.7 eV are assigned to W $4f_{7/2}$ and W $4f_{5/2}$, consistent with the W^{6+} oxidation state in WO_3 [44]. Minor shoulders observed around 36.0 eV and 38.5 eV may be linked to sub-stoichiometric tungsten oxides or intermediate valence states (e.g., W^{5+}), possibly arising from oxygen deficiencies or incomplete oxidation [45]. These features suggest the presence of oxygen vacancies, which can contribute to improved ionic mobility and electrical conductivity.

The O 1 s spectrum (Fig. 5d) is deconvoluted into three distinct components. The peak at 530.5 eV is attributed to lattice oxygen (O^{2-}) bound within the metal oxide matrix [46,47], while the shoulder at ~532.0 eV is commonly associated with surface hydroxyl groups or chemisorbed oxygen species [48,49]. A third component at 533.6 eV is indicative of oxygen within carbonate species or other adsorbed moieties [50,51]. This diversity in oxygen environments reflects a chemically active surface, which may promote electrolyte interaction and improve overall charge storage capacity.

The XPS results confirm that the surface of the WO_3–MnO_2/SiNWs nanocomposite contains mixed-valence states (Mn^{3+}/Mn^{4+} and W^{5+}/W^{6+}) **Table 3**. The predominance of Mn^{4+} and W^{6+} species indicates that annealing at 573 K favors oxidation and structural stabilization of

Table 2
Elemental composition of the WO_3–MnO_2/SiNWs composite obtained from EDX analysis.

Element	Atomic %	Remarks
O	49.2	Oxygen from oxide phases
Mn	17.3	From MnO_2 component
W	16.4	From WO_3 component
Si	17.1	From SiNW substrate
Mn/W ratio	1.05	Close to theoretical 1:1 ratio

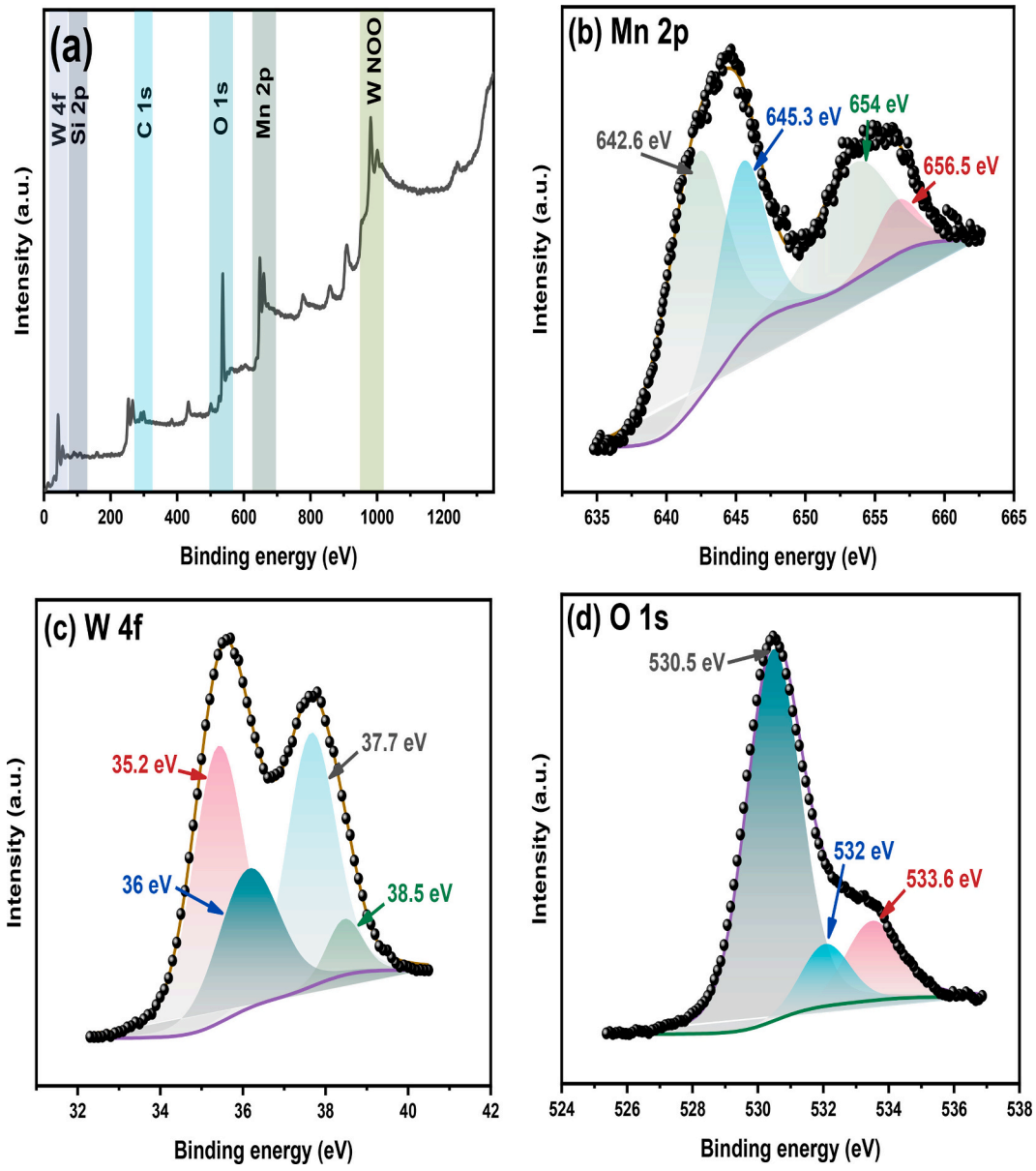

Fig. 5. XPS analysis of the MnO_2/WO_3/SiNWs composite annealed at 573 K: (a) survey spectrum confirming the presence of Mn, W, O, and C; (b) high-resolution Mn 2p spectrum indicating mixed oxidation states of manganese; (c) W 4f core-level spectrum showing tungsten in the W^{6+} oxidation state with possible sub-stoichiometric species; and (d) O 1 s spectrum revealing contributions from lattice oxygen, surface hydroxyl groups, and chemisorbed species.

Table 3
Surface chemical composition and atomic ratios derived from XPS spectra of the MnO_2/WO_3/SiNWs composite (annealed at 573 K).

Element	Oxidation state	Binding energy (eV)	Relative content (%)	Remarks
Mn	Mn^{3+}	654.0, 655.5	43.5	Lower valence, promotes charge storage sites
	Mn^{4+}	642.6, 645.3	56.5	Dominant oxidation state, stable structure
W	W^{5+}	35.2, 37.7	39.8	Sub-stoichiometric species, enhances conductivity
	W^{6+}	36.0, 38.5	60.2	Major component of WO_3 lattice
Mn/W atomic ratio	–	–	~1.05	Nearly equimolar surface composition

the composite. Meanwhile, the presence of Mn^{3+} and W^{5+} contributes to electronic conductivity and provides additional redox-active sites. The nearly equimolar Mn/W ratio (~1.05) suggests a balanced distribution of both transition metals on the surface, which enhances charge storage efficiency and improves electrode stability during cycling. These features correlate well with the improved electrochemical performance observed for this sample, as the coexistence of multiple oxidation states facilitates reversible redox transitions during charge–discharge processes.

Collectively, the XPS data confirm the successful integration of MnO_2 and WO_3 on the SiNW substrate, revealing a complex surface chemistry involving mixed oxidation states and surface functional groups. These features are expected to positively impact the electrochemical performance of the composite by facilitating redox activity and enhancing ion/electron transport.

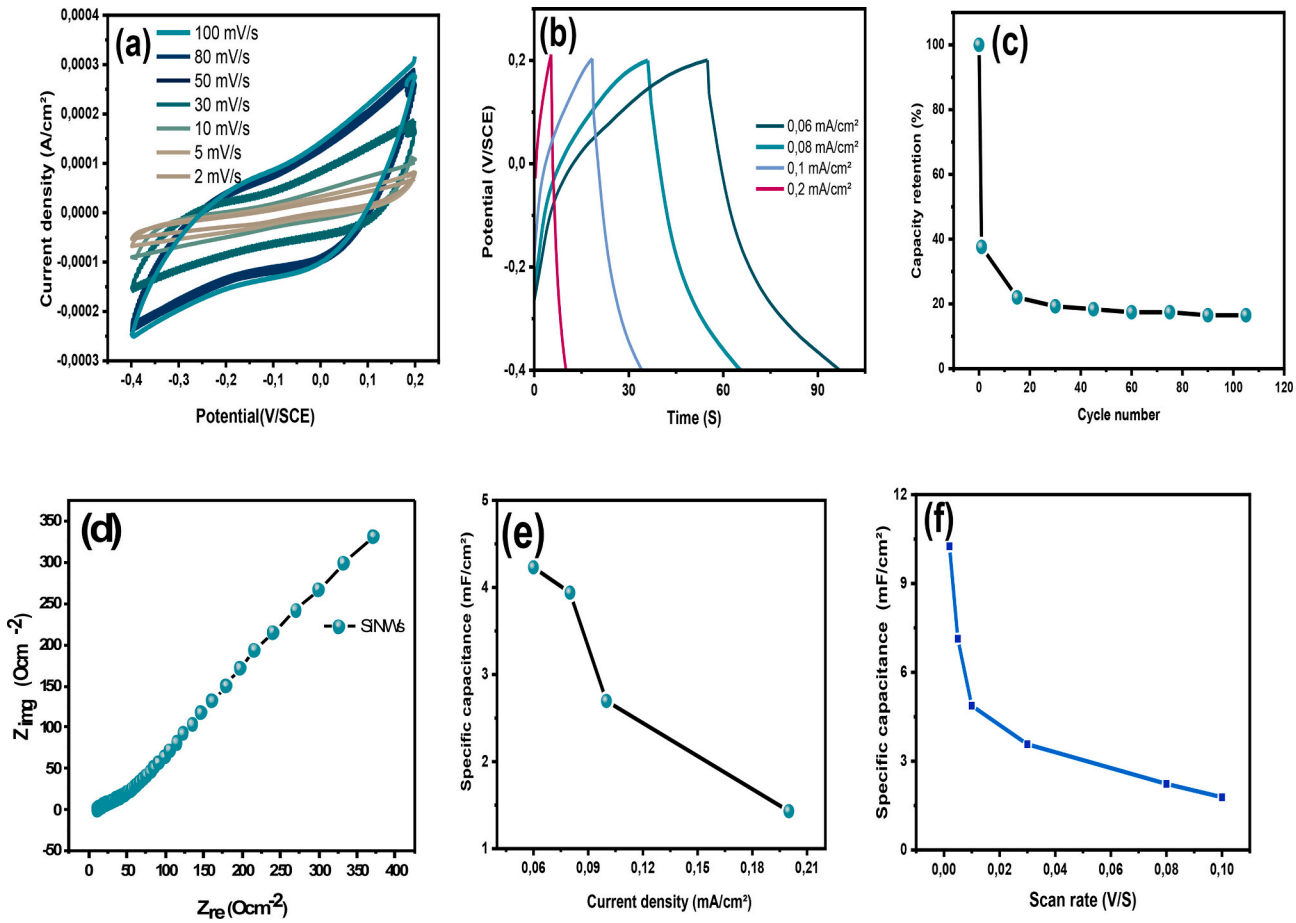

Fig. 6. (a) CV curves of SiNWs/Si electrodes recorded at various scan rates, (b) GCD profiles at different current densities, (c) Capacitance retention as a function of cycle number over 110 cycles, (d) Nyquist plot obtained from EIS, (e) Variation of **Csp** with current density, and (f) Dependence of **Csp** on scan rate.

3.1. Micro-supercapacitor tests

Fig. 6 presents the electrochemical characterization of the SiNWs/Si electrode for micro-supercapacitor (μSC) applications. The cyclic voltammetry (CV) curves shown in Fig. 6a, recorded at varying scan rates (2, 5, 10, 30, 80, and 100 mV/s), exhibit a quasi-rectangular shape across all conditions, which is indicative of ideal capacitive behavior and rapid charge–discharge kinetics. At a scan rate of 2 mV/s, the Csp of the SiNWs/Si electrode was calculated to be approximately 10.25 mF/cm^2. Fig. 6b displays the galvanostatic charge–discharge (GCD) profiles at different current densities (0.06, 0.08, 0.1, and 0.2 mA/cm^2). The nearly symmetric triangular shapes of these curves further confirm the capacitive nature of the electrode. At a current density of 0.06 mA/cm^2, a Csp value of 4.23 mF/cm^2 was achieved, demonstrating enhanced charge storage capability under constant current conditions. Cycling stability was evaluated over 100 charge–discharge cycles, as shown in Fig. 6c, The relatively low cycling stability of the bare SiNWs/Si electrode, which retained only ~20 % of its initial capacitance after 110 cycles, can be attributed to the intrinsic limitations of the silicon nanowire framework when used alone. Although the vertical alignment and high surface area of SiNWs provide efficient electron transport pathways and abundant active sites, their direct exposure to the electrolyte leads to surface oxidation, structural degradation, and partial dissolution during repeated cycling. These effects progressively reduce the number of electrochemically active sites and weaken the electrode integrity, resulting in rapid capacitance fading. This observation highlights the necessity of integrating active oxides such as WO_3 and MnO_2, which serve to passivate the SiNWs surface, enhance redox activity, and significantly improve both cycling stability and overall electrochemical performance. The electrode exhibited a notable decrease in capacitance during the initial cycles, eventually stabilizing at around 20 % of its initial value, which reflects moderate retention under prolonged use. Electrochemical impedance spectroscopy (EIS), presented in Fig. 6d, provides insights into charge transport characteristics. In the high-frequency region, a small semicircle indicates low charge transfer resistance, while the nearly vertical line observed at low frequencies signifies efficient ion diffusion and capacitive behavior. This combination supports the potential of SiNWs/Si structures for rapid energy storage and high-rate performance in μSCs systems.

Fig. 6e illustrates the variation of C_{sp} as a function of current density. As the current density increases, a noticeable decline in C_{sp} is observed, which is consistent with the limited time available for ion diffusion at higher charge–discharge rates. This behavior is typical of supercapacitor electrodes, where only a portion of the active material is effectively utilized under rapid cycling conditions. Similarly, Fig. 6f shows the dependence of C_{sp} on scan rate. The specific capacitance decreases progressively as the scan rate increases, primarily due to reduced ionic penetration into the porous electrode matrix. At higher scan rates, the electrolyte ions have insufficient time to fully access the internal surfaces of the electrode, leading to a lower utilization of the electro active sites.

Overall, these electrochemical tests demonstrate that SiNWs/Si electrodes exhibit promising capacitive behavior, making them suitable for μSC applications. However, improvements in cycling stability and C_{sp} at higher current densities and scan rates are needed to enhance their performance further.

Fig. 7a displays the CV profiles recorded at a scan rate of 50 mV/s within a potential window of −0.4 to 0.2 V vs Ag/AgCl. The

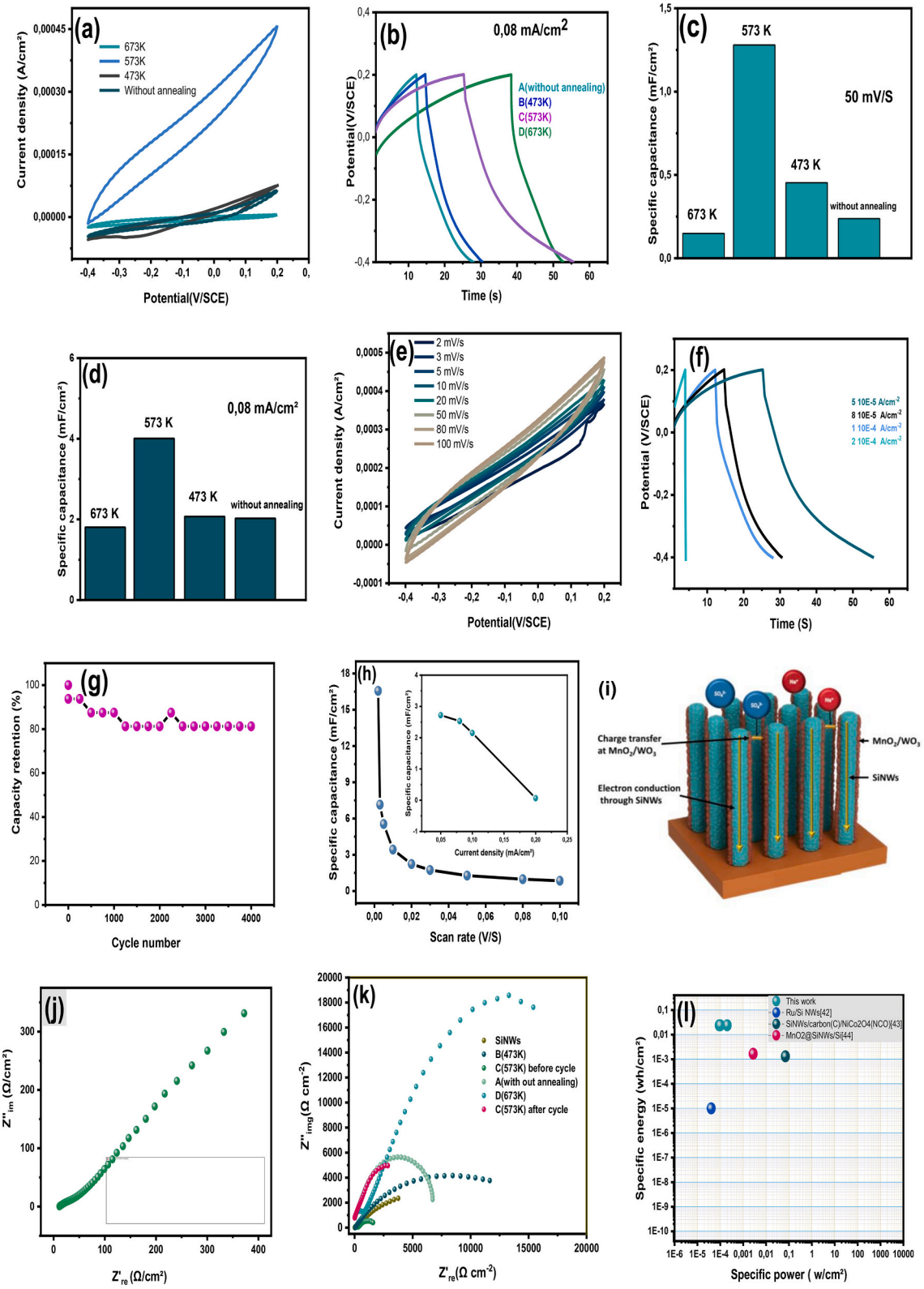

Fig. 7. (a) CV curves comparison of samples A, B, C, and D at a scan rate of 50 mV·s^{-1}; (b) GCD curves of unannealed sample (A) and samples annealed at 473 K (B), 573 K (C), and 673 K (D) at a current density of 0.08 mA·cm^{-2}; (c) comparison of Csp values obtained from CV curves of samples A, B, C, and D at a scan rate of 50 mV·s^{-1}; (d) comparison of Csp values obtained from GCD curves of samples A, B, C, and D at a current density of 0.08 mA·cm^{-2}; (e) CV curves of sample C (annealed at 573 K) at different scan rates; (f) GCD curves at different current densities; (g) plot of capacity retention versus cycle number (1st–4000th cycle) at a current density of 0.1 mA·cm^{-2}; (h) plot of Csp versus scan rate; h-insrt: plot of Csp versus current density; (i) Schematic of the MnO_2/WO_3@SiNWs electrode showing electron conduction through SiNWs and ion diffusion within the oxide coating; (j) Nyquist plot (inset figure shows the equivalent circuit) of sample C before cycling; (k) Nyquist plot comparison of samples A, B, C, D, and C after cycling; and (l) Ragone plot.

enhancement in hybrid electrode performance is attributed to the larger specific surface area, improved electrical conductivity, and the effective intercalation of MnO_2 within the WO_3 matrix. The Csp values for electrodes A, D, B, and C at a scan rate of 0.05 V/s were calculated to be 0.2376, 0.4531, 0.1492, and 1.28 mF/cm^2, respectively. As shown in Fig. 7b, GCD curves exhibit longer discharge durations for electrode C, indicating a higher capacitance of 4.006 mF/cm^2 at 0.08 mA/cm^2. At a current density of 0.08 mA/cm^2, the Csp values for electrodes D, A, B, and C were found to be 1.803, 2.025, 2.075, and 4.006 mF/cm^2, respectively. The non-linear nature of the charge-discharge curves confirms pseudo-capacitive behavior. Fig. 7c presents the Csp variation as a function of scan rate, highlighting that electrode C exhibits the highest capacitance among all tested samples. This finding is further supported by GCD analysis at 0.08 mA/cm^2, as shown in Fig. 7d. The superior performance of electrode C stems from the synergistic interaction between WO_3 and MnO_2, which enhances conductivity and increases the number of available active sites for charge storage. CV curves at scan rates from 2 to 100 mV/s for the WO_3-MnO_2@SiNWs electrode are presented in Fig. 7e. Electrode C achieves a maximum Csp of 16.56 mF/cm^2 at 0.002 V/s, and still maintains 0.853 mF/cm^2 at 0.1 V/s. The absence of a silicon oxidation peak suggests that the silicon core remains chemically stable in the presence of the electrolyte. GCD curves obtained at varying current densities (Fig. 7f) further confirm pseudo-capacitive characteristics. The long-term cycling performance, shown in Figure7, indicates that electrode C retains 84 % of its initial capacitance after 4000 cycles at 0.1 mA/cm^2, demonstrating excellent durability. The observed performance enhancement is largely attributed to the cooperative effect of the WO_3-MnO_2 combination. Figs. 7 h and 7 h-insert illustrate the changes in specific capacitance with different scan rates and current densities. At low scan rates, ions have more time to diffuse into the active material, enabling complete charge/discharge reactions and maximizing the capacitance. In contrast, at high scan rates, insufficient ion diffusion results in lower charge storage efficiency. Similarly, at higher current densities, increased internal resistance and limited ion penetration lead to a drop in capacitance. These effects are primarily due to slower ion transport, incomplete electrochemical reactions, and increased resistance, including electrolyte resistance and IR drop. Fig. 7i presents a schematic illustration of the electron/ion transport pathways within the MnO_2/WO_3@SiNWs electrode. The vertically aligned SiNWs act as highly conductive channels that facilitate rapid electron transport from the current collector to the active material. Simultaneously, the conformal MnO_2/WO_3 coating provides abundant redox-active sites for charge storage, where Na^+ and SO_4^{2-} ions from the electrolyte undergo reversible insertion and extraction. The intimate interface between the SiNWs and the MnO_2/WO_3 layer ensures efficient charge transfer, while the open three-dimensional architecture shortens ion diffusion paths, thereby improving rate capability. This synergistic combination of fast electron conduction through the SiNWs backbone and efficient ion transport within the porous oxide network explains the enhanced capacitive performance and long-term stability of the hybrid electrode. Electrochemical impedance spectroscopy (EIS), presented in Fig. 7j, reveals characteristic semicircles at both high and low frequencies. The data were modeled using an equivalent circuit, and the series resistance (ESR) for electrode C was measured at 8.52 Ω, indicating good electrical properties. The corresponding C_{sp} value was 14.23 mF/cm^2. The Nyquist plots in Fig. 7 k represent the impedance response of the electrodes, showing the real part of the impedance on the x-axis and the imaginary part on the y-axis. A semicircle in the high-frequency region, followed by a tail in the low-frequency region, reflects the charge transfer resistance and diffusion behavior, respectively. Regarding thermal treatment, unannealed electrodes exhibit higher impedance, particularly at high frequencies, due to structural disorder and poor charge mobility. Upon annealing at 473 K and 573 K, enhanced crystallinity and reduced structural defects result in improved charge transfer and lower impedance. However, at 673 K, an increase in impedance is observed again, likely due to structural degradation or grain overgrowth, which reduces the effective surface area. Among all treatments, 573 K offers the best electrochemical performance, as evidenced by the smallest semicircle in the Nyquist plot, indicating an optimal balance of crystallinity, conductivity, and surface reactivity. The Ragone plot in Fig. 7 l reveals that the WO_3-MnO_2@SiNWs electrode achieves a peak energy density of 0.0001 Wh/cm^2 at a current density of 0.1 mA/cm^2. Even under a high-power condition of 0.024 W/cm^2, the electrode maintains strong performance, outperforming conventional SiNWs-based systems [52–54]. This superior behavior results from the formation of 3D nanoparticulate architecture, increased surface area, and the synergistic effects of the binary oxide components, which facilitate efficient ion transport and high charge storage capacity. To evaluate the practical viability of the C-electrode for use in portable electronic devices, a symmetric micro-supercapacitor (μSC) was assembled using two identical C-electrodes. These electrodes were fabricated on 1 × 1 cm^2 SiNWs substrates. Sodium sulfate (Na_2SO_4) served both as the electrolyte and separator in the device, helping to preserve the integrity of the active materials and enhance long-term cycling stability. Fig. 8a illustrates the CV profiles of the symmetric μSC at scan rates ranging from 2 to 100 mV/s within a potential window of −0.5 to +0.5 V. The calculated values for C_{sp}, Ed, and Pd were 96 mF/cm^2. The CV curves are nearly mirror-symmetric across anodic and cathodic sweeps, confirming good pseudo-capacitive behavior. Additionally, their shape remains stable even at high scan rates, indicating excellent rate capability and electrochemical stability. Fig. 8b shows the GCD curves of the symmetric device at different current levels (0.15–2 mA). The near-linear and symmetric shape of the curves confirms efficient charge-discharge behavior and low internal resistance. No significant voltage drop is observed at higher currents, suggesting strong electrical conductivity of the electrode material. At 0.15 mA/cm^2, the device delivered a capacitance of 20.328 mF, 0.0028 Wh/cm^2, and 0.4 W/cm^2, respectively, which remained at 5.952 mF at a higher current density of 2 mA/cm^2. Cycling stability was assessed over 2300 continuous charge-discharge cycles at 0.1 mA/cm^2. As seen in Fig. 8c, the capacitance showed minimal degradation, retaining 84 % of its initial value, which demonstrates the device's robust long-term stability. The corresponding specific capacitance after cycling was found to be 15.88 mF/cm^2. Electrochemical impedance spectroscopy (EIS) was used to further explore the charge transport characteristics. The Nyquist plot in Fig. 8d, recorded across a frequency range of 0.01 Hz to 1 MHz, revealed a series resistance (R_s) of 8.479 Ω and a charge transfer resistance (R_{ct}) of 363.9 Ω/cm^2. The overall specific capacitance derived from impedance data was 20.83 mF/cm^2, indicating favorable electrical performance and efficient ion diffusion within the symmetric micro-supercapacitor.

The porous architecture of electrode C, composed of interconnected nanoparticles, contributes to structural stability and enhances electrochemical performance. As shown in Fig. 8e, the C_{sp} decreases with increasing scan rate, which is attributed to limited time for effective redox reactions at higher rates. The device achieves a peak C_{sp} of 96 mF/cm^2 at a low scan rate of 2 mV/s. The absence of a binder in the electrode design improves electronic conductivity by eliminating insulating barriers. MnO_2 nanoparticles facilitate fast and reversible faradaic reactions and shorten ion diffusion pathways, while WO_3 nanostructures support efficient electron transport [55]. The synergistic integration of MnO_2 and WO_3, each possessing distinct redox states, creates multiple active sites for redox reactions, thereby boosting electrochemical activity. Additionally, the high surface area and mesoporous features of electrode C allow for increased charge storage capacity. As illustrated in Fig. 8f, the specific capacitance tends to decline at higher current densities. This behavior is due to increased internal resistance and the limited time for complete charge-discharge processes, which hampers the electrode's charge storage efficiency. At elevated current loads, the reduced accessibility to electroactive sites results in a noticeable drop in capacitance.

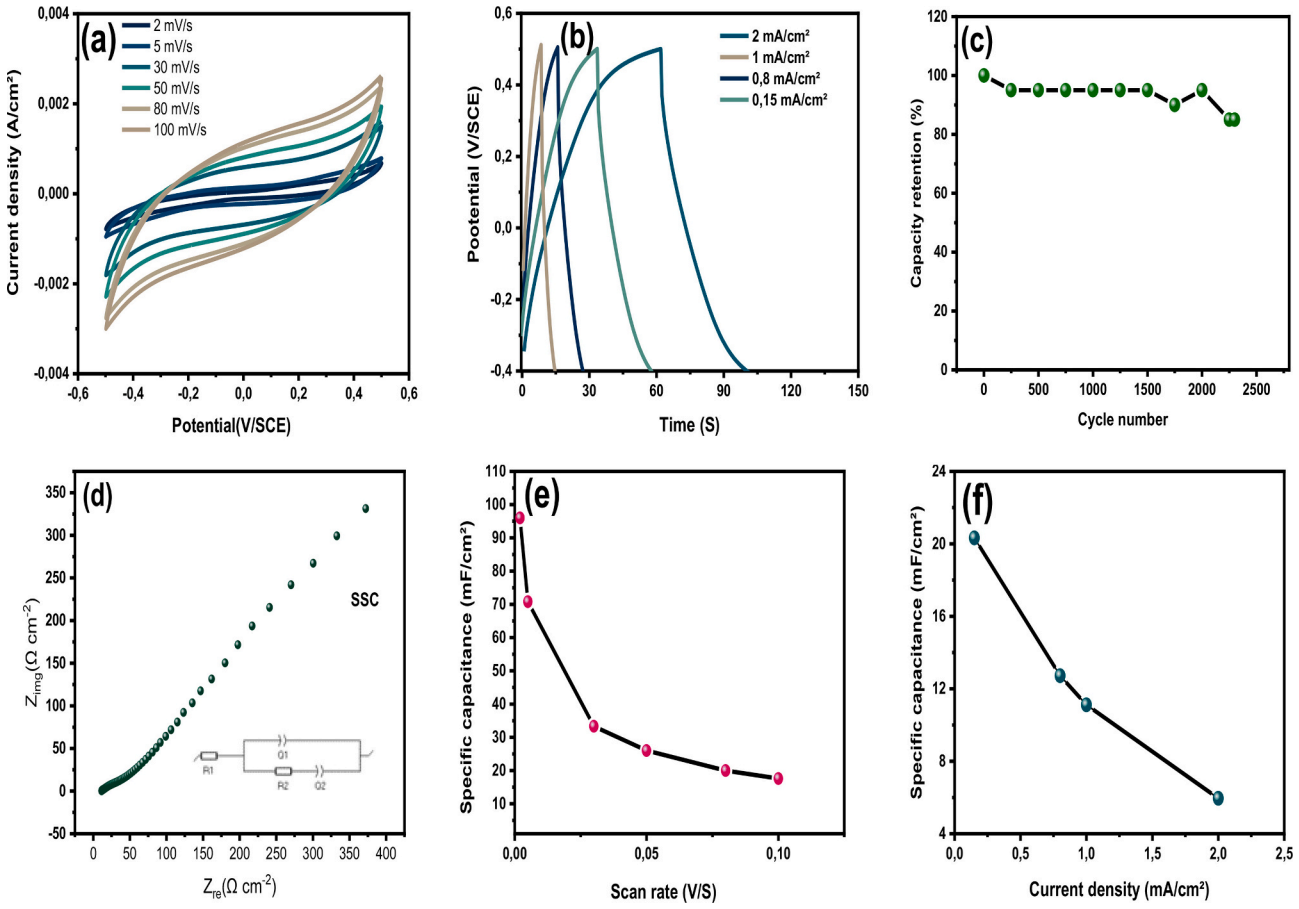

Fig. 8. Electrochemical performance of symmetric μSCs based on WO_3-MnO_2/SiNWs composite electrodes annealed at 573 K: (a) CV curves recorded at various scan rates; (b) GCD curves under different current densities; (c) Capacitance retention over 2300 charge–discharge cycles; (d) Nyquist plot obtained from EIS; (e) C_{sp} as a function of scan rate; (f) Csp variation with applied current density.

4. Conclusion

In this work, WO_3-MnO_2 nanocomposite layers were successfully grown on vertically aligned silicon nanowires (SiNWs) via a simple hydrothermal approach, and their suitability as high-performance electrodes for micro-supercapacitors was systematically evaluated. The combined presence of WO_3 and MnO_2 within the composite structure led to notable improvements in electrochemical behavior, owing to enhanced electrical conductivity and the abundance of redox-active sites. Comprehensive characterization using SEM, EDX, XRD, and XPS confirmed both the successful deposition and the uniform dispersion of the metal oxides on the SiNW framework, highlighting the structural integrity of the composite. Among the different samples studied, the electrode annealed at 573 K (sample C) delivered the most promising performance, achieving a high C_{sp} of 16.56 $mF{\cdot}cm^{-2}$ at 2 $mV{\cdot}s^{-1}$ and maintaining 84 % of its initial capacitance over 4000 charge–discharge cycles. Furthermore, a symmetric solid-state micro-supercapacitor device fabricated with this optimized electrode configuration exhibited a maximum C_{sp} of 96 $mF{\cdot}cm^{-2}$ and sustained 85 % of its capacitance after 2300 cycles, underscoring the structural and electrochemical stability of the system. The excellent performance is attributed to the synergistic interaction between WO_3 and MnO_2, which facilitates rapid electron transport and efficient ion diffusion, as well as to the binder-free integration on the SiNW substrate, which contributes to superior mechanical adherence and enhanced conductivity. These findings demonstrate that the WO_3-MnO_2@SiNWs architecture offers a compelling platform for next-generation micro-scale energy storage devices, combining high energy and power densities with long-term cycling durability. Future research may focus on further optimizing the nanostructure geometry and interface properties to meet the stringent requirements of flexible and portable electronic systems.

CRediT authorship contribution statement

Khadidja Boukhouidem: Writing – original draft, Supervision, Methodology, Data curation, Conceptualization. **Amel Slimani:** Investigation, Formal analysis. **Khaled Derkaoui:** Writing – review & editing, Software, Formal analysis, Data curation. **Theodore Azemtsop Manfo:** Writing – review & editing, Writing – original draft. **Toufik Hadjersi:** Writing – review & editing, Supervision, Resources, Methodology, Conceptualization. **Amar Manseri:** Visualization, Formal analysis. **Noureddine Selmi:** Formal analysis. **Seddik Elhak Abaidia:** Project administration, Formal analysis.

Consent to participate

Not applicable.

Consent for publication

All authors consent to the publication of this manuscript.

Ethics approval

Not applicable.

Funding

This research received no specific grant from any funding agency in the public, commercial, or not-for-profit sectors.

Declaration of competing interest

The authors declare that they have no known competing financial interests or personal relationships that could have appeared to influence the work reported in this paper.

Acknowledgements

This work was financially supported by the Directorate General for Scientific Research and Technological Development (DGRSDT/MESRS), Algeria. The authors also express their sincere gratitude to the staff of the Semiconductor Technology Research Center for Energy (CRTSE), Algeria, for their valuable technical assistance and support.

Appendix A. Supplementary data

Supplementary data to this article can be found online at https://doi.org/10.1016/j.jelechem.2025.119559.

References

[1] A.M. Theodore, A.A. Abbas, P.S. Dhapola, Effect of layered, spinel, and olivine-based positive electrode materials on rechargeable lithium-ion batteries: a review, J. Comput. Mech. Power Syst. Control. 6 (2023) 38–57.
[2] A.M. Theodore, Progress into lithium-ion battery research, J. Chem. Res. 47 (3) (2023) 1–9.
[3] S. Konwar, P.K. Singh, R.M. Mehra, et al., PEO + NaSCN and ionic liquid-based polymer electrolyte for supercapacitor, Mater Today Proc 34 (2021) 802–812.
[4] T.A. Manfo, M.E. Şahin, Intercalation reaction in lithium-ion battery: effect on cell characteristics, Int. J. Mater. Eng. Technol. 6 (2023) 70–78.
[5] N.E. Arabi, Y. Bencheikh, W. Achour, A. Hebbaz, A. Manseri, K. Derkaoui, T. Hadjersi, Facile hydrothermal synthesis of rGO/CoSO4 composite as high-performance supercapacitor electrode: effect of autoclave and non-autoclave, Diam. Relat. Mater. (2025) 112416, https://doi.org/10.1016/J.DIAMOND.2025.112416.
[6] Y.E. Fırat, Pseudocapacitive energy storage properties of rGO-WO_3 electrode synthesized by electrodeposition, Mater. Sci. Semicond. Process. 133 (2021) 105938, https://doi.org/10.1016/J.MSSP.2021.105938.
[7] H. Chen, T.N. Cong, W. Yang, et al., Progress in electrical energy storage system: a critical review, Prog. Nat. Sci. 19 (2009) 291–312.
[8] A. Noori, M.F. El-Kady, M.S. Rahmanifar, et al., Towards establishing standard performance metrics for batteries, supercapacitors, and beyond, Chem. Soc. Rev. 48 (2019) 1272–1341.
[9] J. Jose, V. Thomas, V. Vinod, et al., Nanocellulose-based functional materials for supercapacitor applications, J. Sci.: Adv. Mater. Devices. 4 (2019) 333–340.
[10] K. Tan, S. Heo, M. Foo, et al., An insight into nanocellulose as soft condensed matter: challenge and future prospective toward environmental sustainability, Sci. Total Environ. 650 (2019) 1309–1326.
[11] T.A. Manfo, H. Laaksonen, A review of carbon-based hybrid materials for supercapacitors, New Carbon Mater. 40 (1) (2025) 81.
[12] A.T. Manfo, P.K. Singh, R.M. Mehra, R.C. Singh, M. Gupta, Structural, vibrational, electrical, electrochemical and capacitive investigations on ionic liquid doped P(VDF-HFP)+NaSCN based polymer electrolytes, Recent Innov. Chem. Eng. 14 (1) (2021) 21–34.
[13] Y.A. Kumar, N. Roy, T. Ramachandran, M. Hussien, M. Moniruzzaman, S.W. Joo, Shaping the future of energy: the rise of supercapacitors progress in the last five years, J Energy Storage 98 (2024) 113040, https://doi.org/10.1016/J.EST.2024.113040.
[14] A. Rashid, Review of: "Nano supercapacitors (supercapacitors or electrochemical nanocapacitors)". preprint, 2025, https://doi.org/10.32388/67GWCF.
[15] H. Medjadji, M. Benlembarek, A. Boulahouache, K. Derkaoui, N. Salhi, M. Trari, Novel CoFe2O4 / LaAlO3 nanocomposites: an impressive photocatalyst with p-n hetero-junction for improved H2 generation under visible exposure, Int. J. Hydrog. Energy 88 (2024) 878–887, https://doi.org/10.1016/J.IJHYDENE.2024.09.233.
[16] A. Bencherif, E. Bousbiat, A. Bouraiou, O. Meglali, A. Zoukel, K. Derkaoui, Electrodeposited ZnO sulfurized into ZnS-ZnO composites as a novel approach for cd-free buffer layer in chalcogenide solar cells, Phys. B Condens. Matter 715 (2025) 417611, https://doi.org/10.1016/J.PHYSB.2025.417611.
[17] K. Derkaoui, A. Elfiad, Y. Mebdoua, I. Belkhettab, I. Bencherifa, S. Benredouane, S. Naama, T. Hadjersi, M. Kechouane, Optical and dielectric properties of CuFe2O4 nanoparticles: a pathway to efficient photocatalytic degradation of rhodamine B under visible light, React. Kinet. Mech. Catal. (2025), https://doi.org/10.1007/S11144-025-02906-Z.
[18] I. Bencherifa, I. Belkhettab, O. Dabou, K. Derkaoui, A. Chetoui, A. Manseri, B. Hamdoud, M. Saâd, Facile hydrothermal synthesis of novel Cu0.2Co0.2Zn0.2Mn0.2X (X = Ni0.2, Fe0.2, Ni0.2Fe0.2, Ni0.1Fe0.1) high-entropy alloy nanoparticles with tunable magnetic properties, Mater. Sci. Eng. B 321 (2025) 118526, https://doi.org/10.1016/J.MSEB.2025.118526.
[19] S. Maadadi, M.E.A. Benamar, Y. Mebdoua, K. Derkaoui, F. Lekoui, J.M. Nunzi, H. D. Habak, M. El Ganaoui, N. Belkhalfa, Investigation of optical, dielectric, and electrical properties of ZnO/cold sprayed Al system and their correlation with photovoltaic performance, Opt. Quant. Electron. 576 (57) (2025) 1–27, https://doi.org/10.1007/S11082-025-08266-1.
[20] B. Yang, H. Li, S. Wang, X. Wang, H. Zhang, Multifunctional role of reduced graphene oxide binder for high-performance supercapacitor with commercial-level mass loading, J. Power Sources 454 (2020) 227955, https://doi.org/10.1016/j.jpowsour.2020.227955.
[21] T.A. Manfo, Development, and characterization of a new solid polymer electrolyte for supercapacitor device, Int. J. Electrochem. 2023 (2023) 4825624, https://doi.org/10.1155/2023/4825624.
[22] A. Brik, K. Derkaoui, T. Hadjersi, S. Naama, K. Benfadel, S. Bouachma, S. Benredouane, K. Boukhouidem, Enhanced visible-light photocatalysis via CeO2/NiO heterostructures integrated on silicon nanowires: correlating optical and dielectric properties with methylene blue degradation efficiency, Opt. Quant. Electron. 57 (2025) 551, https://doi.org/10.1007/s11082-025-08459-8.
[23] K. Kahlouche, K. Derkaoui, A. Brik, A. Naitbouda, I. Bencherifa, T. Hadjersi, Tailoring optical and dielectric properties of CeO2/rGO nanocomposites for enhanced Photodegradation of rhodamine B under visible light, J. Electron. Mater. (2025), https://doi.org/10.1007/s11664-025-12448-8.
[24] H. Liu, N. Chen, A. Umar, S. Li, P. Bai, N.F. de Rooij, Y. Wang, G. Zhou, In situ construction of the coral-like polyaniline on the aligned silicon nanowire arrays for silicon substrate on-chip supercapacitors, ACS Appl Energy Mater 3 (12) (2020) 11792–11802, https://doi.org/10.1021/acsaem.0c01963.
[25] K. Derkaoui, I. Belkhettab, I. Bencherifa, A. Elfiad, Y. Mebdoua, K. Boukhouidem, S. Benredouane, S. Naama, T. Hadjersi, M. Kechouane, Optical and dielectric properties of NiFe2O4 prepared by co-precipitation: correlation with photocatalytic performance for rhodamine B degradation under visible light, React. Kinet. Mech. Catal. (2025) 1–19, https://doi.org/10.1007/S11144-025-02861-9.
[26] H. Sun, Y. Miao, G. Wang, X. Han, Y. Wang, Z. Zhang, C. Luo, X. Liu, C. Xu, H. Chen, Sonochemical synthesis of battery-type $ZnCo_2O_4$ electrode material with huge specific surface area for advanced hybrid supercapacitors, J Energy Storage 76 (2024) 109780, https://doi.org/10.1016/J.EST.2023.109780.
[27] Y. Jin, Y. Wang, P.G. Ren, B. Zhang, Z. Zhao, X. Hou, F. Ren, Z. Chen, Z. Guo, H. Yang, X. Li, Recent advances of carbon dots based emerging materials for supercapacitors applications, J Energy Storage 85 (2024) 111118, https://doi.org/10.1016/J.EST.2024.111118.
[28] M. Minakshi, A. Samayamanthry, J. Whale, R. Aughterson, P.A. Shinde, K. Ariga, L. K. Shrestha, Phosphorous-containing activated carbon derived from natural honeydew peel powers aqueous supercapacitors, Chem. Asian J. 19 (2024) e202400622, https://doi.org/10.1002/ASIA.202400622.
[29] A. Soam, K. Parida, R. Kumar, S. All, R. Dusane, Silicon-MnO_2 core-shell nanowires as electrodes for micro-supercapacitor application, Ceram. Int. (2019), https://doi.org/10.1016/j.ceramint.2019.06.127, 45:??–??
[30] M. Xu, Y. Cai, T. Wang, X. Wang, A. Zhou, Z. Yang, Two-dimensional Mg-doped MnO_2@carbon cloth nanosheets for high performance typical flexible solid supercapacitor, J. Alloys Compd. 877 (2021) 160243, https://doi.org/10.1016/j.jallcom.2021.160243.
[31] K. Derkaoui, T. Hadjersi, K. Boukhouidem, et al., Optical, dielectric and photoelectrochemical performances of the CeO_2/silicon nanowire system: studying the silicon nanowire length effect on the photodegradation of rhodamine B, React. Kinet. Mech. Catal. (2024) 1–20, https://doi.org/10.1007/S11144-024-02684-0.
[32] A. Tab, C. Belabed, A. Mahieddine, M.M. Kaci, K. Derkaoui, A. Chetoui, M.S.M. Al-Saleem, A. Khen, L. Adnane-Amara, M. Özacar, T. Hadjersi, A.E. Alsafrani, M. Trari, C. Richard, J.Y. Al-Humaidi, M.M. Rahman, 1T/2H-MoS2@Zn-Ni MOF composite: a novel catalyst for efficient hydrogen production and antimicrobial activity, J Water Process Eng 75 (2025) 108047, https://doi.org/10.1016/J.JWPE.2025.108047.
[33] X. Shen, T. Wang, X. Wei, S. Li, Facile synthesis of metal oxide and conductive polymers around silicon nanowire arrays for a high-performance aqueous supercapacitor, ACS Appl Energy Mater 5 (2022) 2596–2605, https://doi.org/10.1021/ACSAEM.2C00066.
[34] X. Shen, X. Wei, T. Wang, S. Li, H. Li, Solution-processable hierarchical SiNW/PEDOT/MnOx electrodes for high-performance supercapacitors, Mater. Chem. Front. 6 (2022) 2894–2904, https://doi.org/10.1039/D2QM00544A.
[35] X. Shen, X. Wei, T. Wang, S. Li, H. Li, Polypyrrole embedded in nickel-cobalt sulfide nanosheets grown on nickel particles passivated silicon nanowire arrays for high-performance supercapacitors, Chem. Eng. J. 461 (2023) 141745, https://doi.org/10.1016/J.CEJ.2023.141745.
[36] K. Derkaoui, Y. Mebdoua, L. Garagouze, N.E.H. Ahmed Merdoukh, C. Serdani, H. Lahmar, S. Benredouane, N. Bouhelal, N. Abdelyamine, M. Bourahla, T. Hadjersi, Exploring plasma-sprayed MCrAlY and yttria-stabilized zirconia coatings for efficient and scalable hydrogen production, React. Kinet. Mech. Catal. 2025 (2025) 1–17, https://doi.org/10.1007/S11144-025-02914-Z.
[37] X. Li, Y. Zhang, L. Wang, J. Liu, Q. Zhao, Recent advances in high-performance supercapacitor electrode materials: design and mechanisms, J Mater Chem A 10 (2022) 12345–12356, https://doi.org/10.1039/D2TA01234A.

[38] L. Zhao, H. Chen, M. Liu, Z. Huang, K. Xu, Ultrafast and long-life asymmetric supercapacitors based on hierarchical carbon nanostructures, Nano Energy 101 (2023) 107567, https://doi.org/10.1016/j.nanoen.2023.107567.
[39] Y. Chen, W. Li, T. Zhou, S. Wang, D. Wu, Design of porous metal oxide nanosheets for high-performance flexible supercapacitors, Electrochim. Acta 388 (2021) 138682, https://doi.org/10.1016/j.electacta.2021.138682.
[40] F. Moulai, T. Hadjersi, M. Ifires, A. Achour, Enhancement of electrochemical capacitance of silicon nanowires arrays (SiNWs) by modification with manganese dioxide (MnO_2), Silicon 11 (2019) 2799–2810, https://doi.org/10.1007/s12633-019-0066-7.
[41] T.A. Manfo, M.E. Sahin, D.B. Altuntas, Development of quasi-flexible solid polymer blend electrolytes and boron carbide reinforced tea waste electrodes for supercapacitors, J Energy Storage 111 (2025) 115442, https://doi.org/10.1016/j.est.2025.115442.
[42] K. Derkaoui, Y. Mebdoua, A. Djaibet, H. Laiche, C. Serdani, H. Lahmar, S. Benredouane, K. Boukhouidem, N. Abdelyamine, L. Samia, D.H. Hassina, T. Hadjersi, Cold-sprayed copper coatings as novel electrocatalysts for the hydrogen evolution reaction in alkaline medium, React. Kinet. Mech. Catal. (2025), https://doi.org/10.1007/s11144-025-02987-w.
[43] A. Brik, T. Hadjersi, D. Khaled, S. Naama, K. Bendadel, B. Souraya, S. Benredouane, B. Khadija, Tetracycline degradation under visible light using a new SiNW/CeO2/NiO composite as a high-efficiency Photocatalyst, J. Inorg. Organomet. Polym. Mater. (2025) 1–14, https://doi.org/10.1007/S10904-025-03888-0.
[44] K. Derkaoui, I. Bencherifa, A. Elfiad, Y. Mebdoua, I. Belkhettab, K. Boukhouidem, S. Benredouane, T. Hadjersi, A. Manseri, M. Kechouane, Unveiling the optical and dielectric properties of MnFe2O4: a high-performance visible-light Photocatalyst for sustainable rhodamine B degradation, J. Electron. Mater. (2025) 1–16, https://doi.org/10.1007/S11664-025-11991-8.
[45] L. Piliai, T.N. Dinhová, M. Janata, et al., NAP-XPS study of surface chemistry of CO and ethanol sensing with WO_3 nanowires-based gas sensor, Sensors Actuators B Chem. 397 (2023) 134682, https://doi.org/10.1016/J.SNB.2023.134682.
[46] K. Derkaoui, I. Bencherifa, T. Hadjersi, et al., MnO_2 decorated silicon nanowires: a novel photocatalyst for improved rhodamine B removal under visible light exposure, Surf Interfaces 53 (2024) 105086, https://doi.org/10.1016/J.SURFIN.2024.105086.
[47] K. Derkaoui, T. Hadjersi, K. Boukhouidem, et al., Facile CeO_2 nanoparticles deposition on Si-nanowires: application to the rhodamine B photodegradation under visible light, React. Kinet. Mech. Catal. 136 (2023) 1657–1672, https://doi.org/10.1007/S11144-023-02427-7.
[48] N. Bensemmane, H. Medjadji, N. Salhi, A. Boulahouache, K. Derkaoui, A. Skender, Sol–Gel Derived CoAl2O4 Sheets: Synthesis, Characterization, and Photocatalytic Efficiency for Methylene Blue Degradation under Visible Light, ChemistrySelect 10 (2025), https://doi.org/10.1002/SLCT.202502310.
[49] K. Derkaoui, I. Belkhettab, I. Bencherifa, A. Elfiad, Y. Mebdoua, K. Boukhouidem, S. Benredouane, S. Naama, T. Hadjersi, M. Kechouane, Optical and dielectric properties of NiFe2O4 prepared by co-precipitation: correlation with photocatalytic performance for rhodamine B degradation under visible light, React. Kinet. Mech. Catal. (2025) 1–19, https://doi.org/10.1007/S11144-025-02861-9.
[50] Z. Kecira, S. Kaizra, O. Benturki, et al., Synthesis of oxygen-functionalized biomass-based activated carbon as supercapacitor with improved electrochemical performance, Appl. Phys. A Mater. Sci. Process. 129 (2023) 1–12, https://doi.org/10.1007/S00339-023-07141-8.
[51] I. Akkari, Z. Graba, M. Pazos, et al., NaOH-activated pomegranate peel hydrochar: preparation, characterization and improved acebutolol adsorption, Water Air Soil Pollut. 234 (2023), https://doi.org/10.1007/S11270-023-06723-9 (article).
[52] Y. Bencheikh, M. Harnois, R. Jijie, A. Addad, P. Roussel, S. Szunerits, T. Hadjersi, S. E.H. Abaidia, R. Boukherroub, High performance silicon nanowires/ruthenium nanoparticles micro-supercapacitors, Electrochim. Acta 311 (2019) 150–159, https://doi.org/10.1016/j.electacta.2019.04.083.
[53] Z. Eddine Daikh, E.A. Zeitoun, T. Fergoug, Y. Bouhadda, K. Derkaoui, K. Bekki, A. Kadiri, Y. Chaker, M.E.H. El Nokab, C.S. Vojvodin, T. Wang, P.H.M. Van Steenberge, K.O. Sebakhy, Synthesis of shape-controlled silica nanoparticles via dual soft templates: a comparative study between aqueous and microemulsion synthesis for the impregnation of procaine anaesthesia drug, Can. J. Chem. Eng. (2025), https://doi.org/10.1002/CJCE.70087.
[54] I. Bencherifa, I. Belkhettab, A. Chetoui, K. Derkaoui, O. Dabou, S. Latreche, B. Hamdoud, Corrosion characterization of Ti-6Al-4V alloy after constrained groove pressing and TiO2 coating, J. Mater. Eng. Perform. 2025 (2025) 1–21, https://doi.org/10.1007/S11665-025-12091-8.
[55] K. Derkaoui, I. Bencherifa, Y. Mebdoua, K. Boukhouidem, T. Hadjersi, A. Chetoui, S. Naama, S. Friha, M. Kechouane, M.M. Kaci, Novel SiNWs/MnO2/Ni(OH)2 Heterostructure as Photocatalyst for efficient degradation of Rhb under visible light, J. Inorg. Organomet. Polym. Mater. (2024) 1–18, https://doi.org/10.1007/S10904-024-03517-2.